



# CHORUS

This is the accepted manuscript made available via CHORUS. The article has been published as:

## Magnetic anisotropy in ferromagnetic CrI<sub>3</sub>

Lebing Chen, Jae-Ho Chung, Tong Chen, Chunruo Duan, Astrid Schneidewind, Igor Radelytskyi, David J. Voneshen, Russell A. Ewings, Matthew B. Stone, Alexander I. Kolesnikov, Barry Winn, Songxue Chi, R. A. Mole, D. H. Yu, Bin Gao, and Pengcheng Dai

Phys. Rev. B **101**, 134418 — Published 15 April 2020

DOI: [10.1103/PhysRevB.101.134418](https://doi.org/10.1103/PhysRevB.101.134418)

# Magnetic anisotropy in ferromagnetic CrI<sub>3</sub>

Lebing Chen,<sup>1</sup> Jae-Ho Chung,<sup>2,\*</sup> Tong Chen,<sup>1</sup> Chunruo Duan,<sup>1</sup> Astrid Schneidewind,<sup>3</sup> Igor Radelytskyi,<sup>3</sup> David J. Voneshen,<sup>4</sup> Russell A. Ewings,<sup>4</sup> Matthew B. Stone,<sup>5</sup> Alexander I. Kolesnikov,<sup>5</sup> Barry Winn,<sup>5</sup> Songxue Chi,<sup>5</sup> R. A. Mole,<sup>6</sup> D. H. Yu,<sup>6</sup> Bin Gao,<sup>1</sup> and Pengcheng Dai<sup>1,†</sup>

<sup>1</sup>*Department of Physics and Astronomy, Rice University, Houston, Texas 77005, USA*

<sup>2</sup>*Department of Physics, Korea University, Seoul 02841, Korea*

<sup>3</sup>*Forschungszentrum Jülich GmbH, Jülich Centre for Neutron Science (JCNS) at Heinz Maier-Leibnitz Zentrum (MLZ), Lichtenbergstrasse 1, 85748 Garching, Germany*

<sup>4</sup>*ISIS Pulsed Neutron and Muon Source, STFC Rutherford Appleton Laboratory, Harwell Campus, Didcot, Oxon, OX11 0QX, United Kingdom*

<sup>5</sup>*Neutron Scattering Division, Oak Ridge National Laboratory, Oak Ridge, Tennessee 37831, USA*

<sup>6</sup>*Australian Nuclear Science and Technology Organisation, Locked bag 2001, Kirrawee DC, NSW 2232, Australia*

(Dated: March 19, 2020)

We use neutron scattering to show that ferromagnetic (FM) phase transition in the two-dimensional (2D) honeycomb lattice CrI<sub>3</sub> is a weakly first order transition and controlled by spin-orbit coupling (SOC) induced magnetic anisotropy, instead of magnetic exchange coupling as in a conventional ferromagnet. With increasing temperature, the magnitude of magnetic anisotropy, seen as a spin gap at the Brillouin zone center, decreases in a power law fashion and vanishes at  $T_C$ , while the in-plane and  $c$ -axis spin-wave stiffnesses associated with magnetic exchange couplings remain robust at  $T_C$ . We also compare parameter regimes where spin waves in CrI<sub>3</sub> can be described by a Heisenberg Hamiltonian with Dzyaloshinskii-Moriya interaction or a Heisenberg-Kitaev Hamiltonian. These results suggest that the SOC induced magnetic anisotropy plays a dominant role in stabilizing the long range FM order in single layer 2D van der Waals ferromagnets.

## I. INTRODUCTION

Understanding the microscopic origin of two-dimensional (2D) ferromagnetic (FM) order and spin dynamics in van der Waals materials is important for their potential magnet-based applications<sup>1</sup>. In a conventional three-dimensional (3D) cubic spin-rotation invariant (spin isotropic) ferromagnet, the Curie temperature  $T_C$  associated with the second order FM phase transition is determined by the short range magnetic exchange coupling  $J^2$ . In the low wave-vector ( $q \rightarrow 0$ ) limit, spin-wave energies  $E$  follow the well-known quadratic dispersion relation  $E = \Delta(T) + D(T)q^2$ , where  $D(T)$  [ $D(T \rightarrow 0) \propto J$ ] is the spin-wave stiffness and  $\Delta(T)$  is a vanishingly small dipolar gap<sup>2</sup>. The quadratic dispersion form, however, is general for any ferromagnet and not limited to the Heisenberg model<sup>2</sup>. According to the hydrodynamic and mode-mode coupling theories, temperature dependence of the spin-wave stiffness in a second order FM phase transition must vanish at  $T_C$  via  $D(T) \propto (1 - T/T_C)^{\nu-\beta}$ , where  $\nu$  and  $\beta$  are critical exponents of the magnetic phase transition<sup>3,4</sup>. For a typical 3D Heisenberg ferromagnet, we expect  $(\nu - \beta) = 0.34$  comparing with the measured values for iron ( $0.36 \pm 0.03$ ), cobalt ( $0.39 \pm 0.05$ ), and nickel ( $0.39 \pm 0.04$ )<sup>4</sup>. When the dimensionality of the magnetic system is reduced from 3D to 2D, Mermin and Wagner showed the absence of long-range FM or antiferromagnetic (AF) order at finite temperature in spin-rotational invariant systems with short-range magnetic interactions<sup>5</sup>. Although the long-range FM order in 2D systems at finite temperature can be brought

about by breaking the spin-rotational invariance<sup>6</sup>, the ordering temperature is again expected to be determined by  $J$ , resulting  $D(T) \rightarrow 0$  at  $T_C$ <sup>1,4,6,7</sup>. Therefore, the discovery of robust FM order in van der Waals monolayers of CrI<sub>3</sub><sup>8</sup> and Cr<sub>2</sub>Ge<sub>2</sub>Te<sub>6</sub><sup>9</sup> raised an important question concerning the magnetic interactions that break the spin-rotational invariance and stabilize the finite temperature 2D FM order.

In principle, spin rotational invariance of a 3D magnetic system can be broken via dipolar interactions<sup>10</sup>, single-ion (magnetocrystalline) anisotropy<sup>11</sup>, and/or anisotropic magnetic exchange interactions<sup>12,13</sup>. For layered honeycomb lattice ferromagnet such as CrI<sub>3</sub> [Figs. 1(a,b)]<sup>14</sup>, another possible mechanism that can break spin rotational invariance is the off-diagonal term  $\Gamma$  in the Heisenberg-Kitaev ( $J$ - $K$ - $\Gamma$ ) Hamiltonian [Fig. 1(c)]<sup>15-23</sup>. For bulk CrI<sub>3</sub>, which orders ferromagnetically below  $T_C = 61$  K, the FM order is believed to be a second order phase transition<sup>14</sup>. In addition, there is a strong magnetic anisotropy revealed as a large difference in the saturation magnetic field for field parallel to the  $c$ -axis direction ( $H_c^S$ ) and in the  $ab$  plane ( $H_{ab}^S$  and  $H_{ab}^S - H_c^S \approx 3$  T)<sup>14,24</sup>. By comparing the temperature dependence of the magnetic anisotropy of CrI<sub>3</sub> with those of CrBr<sub>3</sub>, it was concluded that the magnetic anisotropy in CrI<sub>3</sub> arises from a dominant uniaxial or single-ion anisotropy<sup>24</sup>, which comes mostly from the interplay between spin-orbit coupling (SOC) of the Cr magnetic ion with the crystal electric field (CEF) levels induced by its surrounding I atoms arranged in an edge sharing octahedra [Figs. 1(c,d)]. Since dipolar interactions typically are very small and favor in-plane anisotropy<sup>10</sup>, its effects on

spin rotation anisotropy is negligible and can be safely ignored<sup>12,13</sup>. On the other hand, single-ion anisotropy in CrI<sub>3</sub> has been estimated to be way below 1 meV because of the quenched orbital moment of Cr<sup>3+</sup> and the large energy separation ( $\approx 500$  meV) of the CEF excited states of the Cr<sup>3+</sup> ion [Figs. 1(c,d)]<sup>12,13</sup>. Finally, spin rotational invariance of a magnetic system such as CrI<sub>3</sub> can be broken because of the magnetic anisotropy arising from the Cr 3*d*-I *p*-Cr 3*d* superexchange hopping in the near 90° bonding angle networks [Fig. 1(c)]<sup>12,13</sup>.

If magnetism in 3D CrI<sub>3</sub> also breaks the spin rotational invariance and becomes anisotropic in real space, it should reveal itself as a gap in spin-wave dispersion at the  $\Gamma$  point in Fig. 1(b) with  $\Delta > 0$ , in contrast to the  $\Delta \approx 0$  seen in typical isotropic ferromagnets<sup>25,26</sup>. In principle, one can detect such a gap by FM resonance<sup>27</sup>, Raman scattering<sup>28</sup>, or inelastic neutron scattering (INS)<sup>25,26</sup>. Using FM resonance<sup>29</sup>, a spin gap of  $\sim 0.3$  meV was estimated at the  $\Gamma$  point below  $T_C$ <sup>18</sup>. On the other hand, polarized micro-Raman spectroscopy experiments on CrI<sub>3</sub> found evidence for two sets of zero wave-vector spin waves at 9.4 meV and 15.5 meV<sup>30</sup>. Since CrI<sub>3</sub> has two magnetic ions per unit cell, giving rise to only one acoustic and one optical spin-wave branches<sup>18,30,31</sup>, the Raman spectroscopy results suggest a spin gap of 9.4 meV at the  $\Gamma$  point<sup>30</sup>. Finally, INS experiments on single crystals of CrI<sub>3</sub> revealed a  $\sim 4$  meV spin gap at the Dirac (*K*) points but found no evidence of a spin gap above  $\sim 1$  meV at the  $\Gamma$  point<sup>31</sup>. While FM resonance<sup>18</sup> and INS<sup>31</sup> results are clearly in contrast to those of Raman spectroscopy<sup>30</sup>, the actual value of the anisotropy gap is still undetermined. To conclusively determine the size of the spin gap and its temperature dependence, and test if spin dynamics in CrI<sub>3</sub> are consistent with a Heisenberg ferromagnet<sup>4</sup>, INS experiments are necessary.

## II. RESULTS

In this paper, we report INS studies of spin waves in CrI<sub>3</sub>. In addition to confirming a spin gap of  $\Delta = 0.37 \pm 0.02$  meV at  $T = 3$  K and the  $\Gamma$  point, we trace the temperature dependence of  $\Delta(T)$  and  $D(T)$  across  $T_C$ . While spin-wave stiffness within the CrI<sub>3</sub> plane  $D_{HH}(T)$  is considerably larger than that of the stiffness along the *c*-axis  $D_L(T)$ , they both do not vanish at  $T_C$ , contrary to the expectation of a 3D<sup>3,4</sup> or 2D<sup>1,6,7</sup> Heisenberg ferromagnet with a second order FM phase transition. On the other hand, the anisotropy gap  $\Delta(T)$  has an order-parameter-like temperature dependence and vanishes at  $T_C$ . These results, together with the lack of magnetic critical scattering around  $T_C$ , suggest that the FM phase transition in CrI<sub>3</sub> is weakly first order instead of a second order phase transition. We thus conclude that the breaking of the spin-rotation invariance via large SOC is ultimately responsible for stabilizing the FM order in 3D and monolayer CrI<sub>3</sub>, and other monolayer materials<sup>32-36</sup>.

We carried out some of the measurements using the

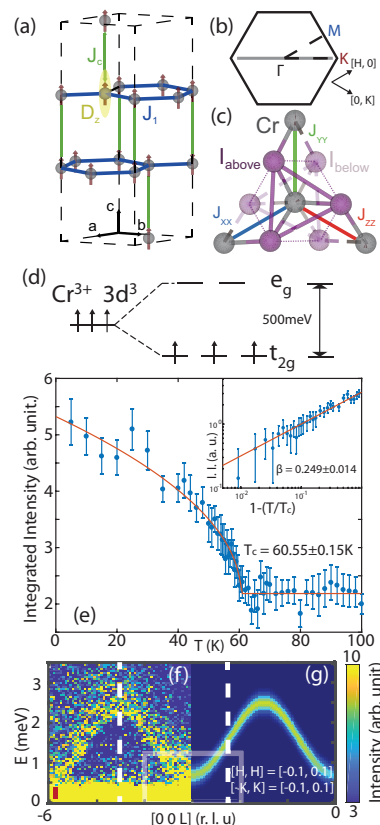


FIG. 1. (a) Crystal structure of CrI<sub>3</sub>, where the nearest neighbor magnetic exchange couplings within the Cr-plane and along the *c*-axis are  $J_1$  and  $J_c$ , respectively. The  $D_z$  is the single-ion anisotropy. (b) Reciprocal space within the [*H*, *K*] plane, where  $\Gamma$ , *K*, *M* points are specified. The gray line indicates the  $\mathbf{Q}$ -direction for constant-energy scans. (c) Real space picture of CrI<sub>3</sub>, where the nearest-neighbor I atoms form an octahedral environment with 3 I above (dark purple) and 3 I below (light purple) the Cr layer. The Cr-I-Cr path forms an angle close to 90 degrees<sup>12,13</sup>. The Kitaev interactions between Cr<sup>3+</sup> atoms are marked as  $J_{xx}$ ,  $J_{yy}$ , and  $J_{zz}$ <sup>18</sup>. (d) The CEF level of the I octahedra splits the *d* levels in the  $e_g$  and  $t_{2g}$  manifolds. (e) Magnetic order parameter at the (1, 1, 0) position. The inset is a log-log plot of the integrated magnetic peak intensity. Both red lines are power law fits with the same critical exponent  $\beta = 0.249 \pm 0.014$ . (f) Spin-wave dispersion along the [0, 0, *L*] direction at  $T = 3$  K obtained with  $E_i = 5.2$  meV. (g) The Heisenberg model fit of the *c*-axis dispersion. The dashed lines in (f,g) indicate constant- $\mathbf{Q}$  scans in Figs. 2(c,d). Red bars in (f), Figs. 2(a,c,d,e), 3(e), and 4(a) are instrumental energy resolution<sup>23</sup>.

LET neutron time-of-flight chopper spectrometer at Rutherford-Appleton Laboratory, Didcot, UK<sup>37</sup>. The experiments were carried out with multi- $E_i$  (incident beam energy) mode ( $E_i = 25$  meV, 5.37 meV [Fig. 1(f)] and 2.27 meV [Fig. 2(a,b)]) with single crystals of CrI<sub>3</sub> fixed at  $T = 3$  K. A Horace scan was done on co-aligned 0.42 g single crystals of CrI<sub>3</sub> with the sample in the [*H*,*H*,*L*] scattering plane<sup>38</sup>. Using a honeycomb structure with in-plane Cr-Cr distance of  $a = b \approx 3.96$  Å and *c*-axis

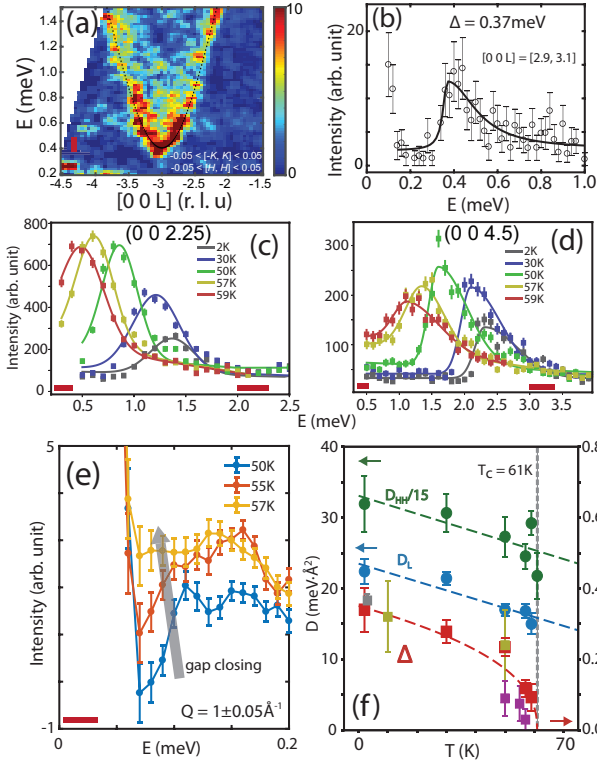


FIG. 2. (a) Images of spin waves near the  $\Gamma$  point. The red box shows the integration range in (b). (b) An energy cut of the data at  $\mathbf{Q} = (0, 0, -3)$ . (c) Constant- $\mathbf{Q}$  scans for  $\mathbf{Q} = (0, 0, 2.25)$ . (d) Similar scans at  $\mathbf{Q} = (0, 0, 4.5)$ . (e) Temperature dependence of the spin gap around the  $\Gamma$  point<sup>23</sup>. (f) Temperature dependence of the  $D_{HH}(T)$  (green dots),  $D_L(T)$  (blue squares), and  $\Delta(T)$  (different colored squares), where the dashed line is a fit to the power law equation. The green and blue dashed lines are guides to the eye.

layer spacing of  $c = 6.62 \text{ \AA}$  in the low temperature rhombohedral structure [Fig. 1(a)]<sup>39</sup>, the momentum transfer  $\mathbf{Q} = H\mathbf{a}^* + K\mathbf{b}^* + L\mathbf{c}^*$  is denoted as  $\mathbf{Q} = (H, K, L)$  in reciprocal lattice units (r.l.u.) [Fig. 1(b)]<sup>31</sup>.

We have also carried out inelastic neutron scattering experiments on the cold neutron triple-axis spectrometer PANDA at Heinz Maier-Leibnitz Zentrum, Garching, Germany [Figs. 2(c,d)]<sup>40</sup>. The experiments were carried out with a fixed final neutron energy of  $E_f = 3.78 \text{ meV}$ . Constant- $E$  scans were performed along the  $[H, H, 3]$  direction at temperatures of 2 K, 30 K, 50 K, 57 K, 59 K, 61 K, 63 K, 68 K, 73 K, 78 K, 84 K, and 250 K. Constant- $\mathbf{Q}$  scans are performed at  $\mathbf{Q}_{2.25} = (0, 0, 2.25)$  and  $\mathbf{Q}_{4.5} = (0, 0, 4.5)$  with sample temperatures of 2 K, 30 K, 50 K, 57 K and 59 K [Figs. 2(c,d)]. The sample mass is 0.84 g of co-aligned single crystals of  $\text{CrI}_3$ . To get the anisotropy gap  $\Delta$  and  $D_L$  along  $c$ -axis, which is related to the spin-wave bandwidth  $E_{band}$  along the  $[0, 0, L]$  direction, we used  $E_{band} = 2(E_{\mathbf{Q}_{4.5}} - E_{\mathbf{Q}_{2.25}})$ , and  $\Delta = E_{\mathbf{Q}_{4.5}} - E_{band}$  to estimate the values of  $D_L$  and  $\Delta$  in Fig. 2(f).

To accurately determine the temperature dependence

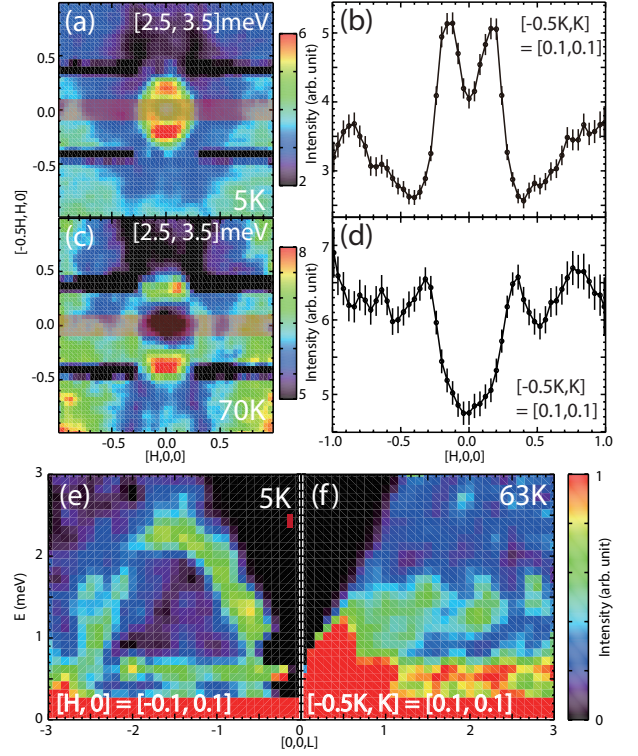


FIG. 3. (a) Low energy ( $E = 3 \pm 0.5 \text{ meV}$ ) spin waves of  $\text{CrI}_3$  in the  $[H, K]$  plane at  $T = 5 \text{ K}$ . (b) A cut along the  $[H, 0]$  direction. (c) The same scan as (a) but at  $T = 1.14T_C$ . (d) The same cut as (b) at  $T = 1.14T_C$ . The red boxes in (a,c) show the integration range in (b,d), respectively, with  $L$  integrated from  $[-5, 5]$ . (e) Spin wave dispersion along the  $c$ -axis at  $T = 5 \text{ K}$ . (f) Identical scan at  $T = 1.03T_C$ . The data was collected using  $E_i = 8 \text{ meV}$ <sup>23</sup>.

of the gap  $\Delta(T)$  at  $\Gamma$  point, we carried out INS measurements using the Pelican neutron time-of-flight spectrometer at ANSTO, Australia [Figs. 2(e,f)]<sup>41</sup>. These experiments were performed on 14 g powder samples of  $\text{CrI}_3$  at 2 K, 50 K, 55 K and 57 K. Two incident energies,  $E_i = 3.7$  and  $2.3 \text{ meV}$ , were used to probe the anisotropy gap  $\Delta(T)$  located at  $\mathbf{Q} = (0, 0, 3)$  (corresponding to  $q_{gap} = 0.96 \text{ \AA}^{-1}$ ). The anisotropy gap value  $\Delta(T)$  is extracted by subtracting the integrated intensity in the range  $(q_{gap} - 0.05) - (q_{gap} + 0.05) \text{ \AA}^{-1}$  by an average of the intensity in the range  $(q_{gap} - 0.35) - (q_{gap} - 0.25) \text{ \AA}^{-1}$  and  $(q_{gap} + 0.25) - (q_{gap} + 0.35) \text{ \AA}^{-1}$ <sup>23</sup>.

Our experiments on neutron time-of-flight chopper spectrometer SEQUOIA at spallation neutron source, Oak Ridge National Laboratory (ORNL), Oak Ridge, Tennessee<sup>42</sup>, were carried out with  $E_i = 25 \text{ meV}$  [Fig. 3(a-d)] and  $8 \text{ meV}$  [Fig. 3(e,f)] at temperatures 5 K, 52 K, 63 K, and 70 K<sup>23</sup>. Horace scans are done on co-aligned 0.2 g single crystals of  $\text{CrI}_3$  with the sample in the  $[H, 0, L]$  scattering plane. The 0.6 meV flat mode in Figs. 3(e,f) is an instrumental artifact.

The magnetic critical scattering is measured on the HB-3 thermal neutron triple-axis spectrometer at

High-Flux Isotope Reactor, ORNL [Figs. 4(a-g)]. The monochromator, analyzer, and filter are pyrolytic graphite (PG). For triple-axis measurements, final neutron energy of  $E_f = 14.7$  meV was used and a PG filter was placed after the sample. For two-axis measurements, a PG filter was placed before the sample to reduce  $\lambda/2$  and incident neutron energy was set at  $E_i = 30.5$  meV. A single piece of  $\text{CrI}_3$  single crystal (13 mg) with mosaic  $\approx 1$  degree was used in the experiment. The HYSPEC experiments<sup>43</sup> were performed on 6 g powder samples at 3 K [Fig. 5(a)]. A Horace scan is performed to eliminate the anisotropy inside the powder sample.

In an ionic picture,  $\text{Cr}^{3+}$  in  $\text{CrI}_3$  has an electronic configuration  $3s^03d^3$  and is surrounded by 6 I atoms in an octahedral environment [Fig. 1(c)]. The  $d$  levels of  $\text{Cr}^{3+}$  split into a higher energy  $e_g$  doublet and a lower energy  $t_{2g}$  triplet separated by  $\sim 500$  meV [Fig. 1(d)]<sup>12</sup>. With the first Hund rule, 3 electrons in  $\text{Cr}^{3+}$  occupy the  $t_{2g}$  manifold in the  $S = 3/2$  state with quenched orbital moment  $\langle \vec{L} \rangle \simeq 0$  [Fig. 1(d)]<sup>12,13</sup>. Figure 1(e) shows temperature dependence of the (1, 1, 0) Bragg peak intensity, confirming the FM transition at  $T_C = 60.5 \pm 0.2$  K. The solid line in the figure is a fit to the magnetic order parameter by  $I = I_0(1 - T/T_C)^{2\beta}$ . Within the temperature range probed, we find  $\beta = 0.25 \pm 0.01$  [Inset in Fig. 1(e)]. This value is in-between the critical exponents of 2D and 3D Ising ferromagnets<sup>4,44</sup>, thus suggesting finite interplanar ( $c$ -axis) magnetic exchange coupling  $J_c$  in  $\text{CrI}_3$ . This is consistent with the spin-wave dispersion along the  $c$ -axis at  $T \approx 3$  K [Fig. 1(f)]. Figure 1(g) shows a fit to the spin-wave dispersion using a Heisenberg Hamiltonian<sup>31</sup>.

Figure 2(a) shows spin waves near the  $\Gamma$  point, revealing an anisotropy gap of  $\Delta = 0.37 \pm 0.02$  meV at  $T = 3$  K. An energy cut at the spin-wave minimum indicates step-like intensity gain around 0.37 meV [Fig. 2(b)]. While the magnitude of  $\Delta$  is smaller by a factor of two compared with estimation from previous measurements<sup>31</sup>, it is consistent with estimation from the FM resonance<sup>18,29</sup> and larger than in its isostructural compound  $\text{CrBr}_3$  ( $\Delta < 0.1$  meV)<sup>45</sup> and  $\text{CrSiTe}_3$  ( $\Delta \approx 0.075$  meV)<sup>46</sup>, suggesting considerably stronger SOC in  $\text{CrI}_3$ .

To determine the temperature dependence of the magnetic exchange couplings within the  $\text{CrI}_3$  plane and along the  $c$ -axis, we measured spin-wave dispersions around the  $\Gamma$  point along the intraplanar  $[H, H, 3]$ <sup>23</sup> and interplanar  $[0, 0, L]$  directions. Figures 2(c,d) are the constant- $\mathbf{Q}$  scans to probe the temperature dependence of interplanar modes for temperatures up to  $T = 59$  K ( $= 0.97T_C$ ). Since the full interplanar spin-wave bandwidth could be observed [Fig. 1(f)], we performed variable-energy scans at  $\mathbf{Q} = (0, 0, 2.25)$  [Fig. 2(c)] and  $(0, 0, 4.5)$  [Fig. 2(d)]. The zone boundary spin-wave energy at  $T = 0.97T_C$  is reduced by  $\sim 50\%$  [Fig. 2(d)], suggesting significant interplanar exchanges approaching the FM transition. Assuming that the interplanar dispersion follows the simple sinusoidal dependence on  $L$  [Fig. 1(f)], we can estimate the spin wave stiffness along the  $c$ -axis  $D_L(T) \equiv a_L(T)(c/6)^2$  in units of  $\text{meV}\text{\AA}^2$  by fitting the

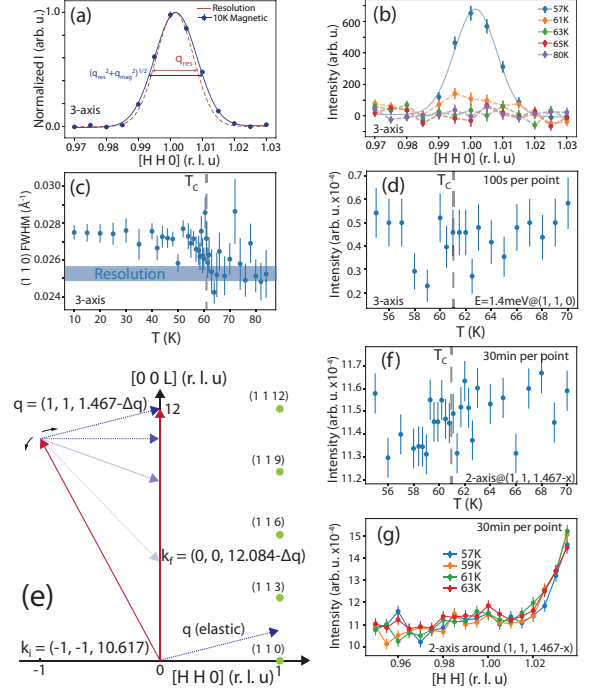


FIG. 4. (a) Wave vector dependence of the magnetic Bragg peak (1, 1, 0) along the  $[H, H, 0]$  direction obtained by subtracting the nuclear Bragg peak above  $T_C$  from the same scan at 10 K. The dashed line is the instrument resolution limited nuclear Bragg peak above  $T_C$  (80 K to 84 K). The data was collected on HB-3 with collimation of  $40'-40'-40'-120'$  and final neutron energy of  $E_f = 14.7$  meV. The blue line is a fit to Gaussian on a flat background, giving spin-spin correlation length of  $220 \pm 4$   $\text{\AA}$ . (b) Temperature dependence of the magnetic scattering around the (1, 1, 0) position across  $T_C$ , where high temperature nuclear Bragg peak is subtracted. (c) Temperature dependence of the full-width-half-maximum (FWHM) of the (1, 1, 0) peak across  $T_C$ . Above  $T_C$ , the FWHM shows instrumental resolution limited nuclear Bragg peak width. (d) Temperature dependence of the inelastic scattering at  $E = 1.4$  meV and (1, 1, 0). (e) Schematics of the two-axis mode scan with neutron final wave vector  $k_f || c$ . The incident neutron energy  $E_i$  is fixed at 30.5 meV. The scattering intensity shown in (f) and (g) is integrated over all possible  $k_f$ . (f) Temperature dependence of the scattering at in-plane wave vector (1, 1, 0). (g)  $[H, H, 0]$  scans across the in-plane wave vector (1, 1, 0) around  $T_C$  using two-axis mode. The intensity obtained in (f) and (g) is an integration over all possible values of  $\Delta q$ .

data with  $E = a_L(T) [\sin(\frac{\pi}{3}L)]^2 + \Delta(T)$ . Figure 2(e) shows temperature dependence of spin gap around the  $\Gamma$  point ( $|\mathbf{Q}| = 1 \pm 0.05$   $\text{\AA}^{-1}$ ) approaching  $T_C$ <sup>23</sup>. Figure 2(f) summarizes temperature dependence of the in-plane  $[D_{HH}(T)]$ <sup>23</sup> and  $c$ -axis  $[D_L(T)]$  spin wave stiffnesses, revealing that the intraplanar and interplanar exchange couplings almost fully active up to  $T_C$  in spite of the vanishing magnetization at  $T_C$  in Fig. 1(e). In contrast,  $\Delta(T)$  obtained from the  $c$ -axis dispersion and di-

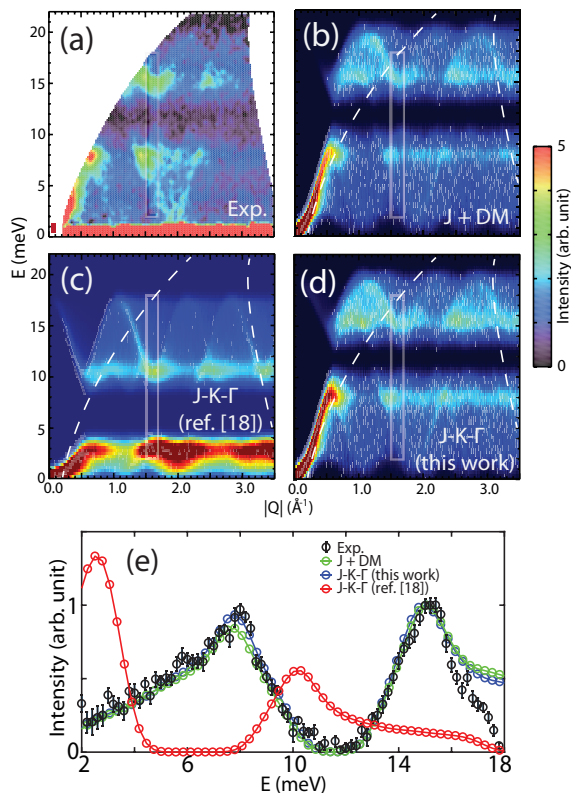


FIG. 5. (a) INS data of the  $\text{CrI}_3$  powder at  $T = 5$  K using  $E_i = 25$  meV. (b,c,d) Powder-averaged spin-wave spectra calculated using the Heisenberg-DM<sup>31</sup>,  $J$ - $K$ - $\Gamma$  Hamiltonian using parameters of Ref.<sup>18</sup>, and new parameters ( $J_1 = -0.17 \pm 0.05$  meV,  $J_2 = -0.21 \pm 0.04$  meV,  $K = -5.6 \pm 0.2$  meV), respectively. The dashed lines mark the limits of the data in (a). (e) The black, green, red, and blue points/lines are the experimental data, Heisenberg-DM,  $J$ - $K$ - $\Gamma$  Hamiltonian calculations with parameters of Ref.<sup>18</sup> and the new parameters mentioned above, respectively. The scan directions are marked as solid boxes in (a-d).

rect measurements vanishes at  $T_C$  [see right axis in Fig. 2(f)]<sup>23</sup>. The dashed line shows a fit to the data using  $\Delta(T) \propto (1 - T/T_C)^{\nu-\beta}$ , giving  $\nu - \beta = 0.35 \pm 0.14$ .

At temperatures above  $T_C$ , spin excitations of  $\text{CrI}_3$  become diffuse but still have signatures of the intraplanar modes. Figures 3(a) and 3(c) are images of the constant-energy slices ( $E = 3.0 \pm 0.5$  meV) at  $T = 5$  K and 70 K, respectively<sup>23</sup>. We see clear spin-wave-like rings in the  $[H, K]$  plane at both temperatures although the excitations are noticeably diffusive at  $T = 70$  K ( $= 1.14T_C$ ).  $Q$ -dependent cuts through data in Figs. 3(b) and 3(d) bear this out, showing some softening of the in-plane spin-wave energy on warming but is non-vanishing at  $T_C$ . Figures 3(e) and 3(f) show similar data along the  $c$ -axis, where we see considerable yet incomplete ( $\sim 50\%$ ) softening of the mode above  $T_C$ . Therefore, FM order in  $\text{CrI}_3$  is not determined by the in-plane or  $c$ -axis magnetic exchange interactions as in a conventional 3D Heisenberg ferromagnet<sup>4</sup>. It is also different from the expectation of

an ideal 2D Heisenberg ferromagnet<sup>1,6,7</sup>.

To understand why  $D(T)$  does not vanish at  $T_C$  in  $\text{CrI}_3$  as required by the mode-mode coupling theory in a Heisenberg ferromagnet with second order phase transition<sup>4</sup>, we consider the nature of the FM phase transition. In a second order FM phase transition, spin-spin correlation length and magnetic critical scattering should diverge at  $T_C$ <sup>4</sup>. Figure 4(a) compares the magnetic Bragg peak across the  $(1, 1, 0)$  reflection at 10 K with the instrumental resolution obtained by measuring the same nuclear Bragg peak above  $T_C$ . The magnetic Bragg peak width is clearly broader than the nuclear Bragg peak width, indicating that the spin-spin correlation length is not resolution-limited. Temperature dependence of the magnetic scattering around the  $(1, 1, 0)$  reflection in triple-axis mode reveals no peak above  $T_C$  [Fig. 4(b)], suggesting the lack of critical scattering around  $T_C$ . Figure 4(c) shows temperature dependence of the  $(1, 1, 0)$  peak width. At temperatures above  $T_C$ , the  $(1, 1, 0)$  peak width measures nuclear lattice correlation, which is the instrumental resolution-limited. On cooling below  $T_C$ , we see a clear broadening of the width that saturates below about 53 K, indicating that the in-plane spin-spin correlations in  $\text{CrI}_3$  are short-ranged even at 10 K and never reached the instrumental resolution (nuclear Bragg peak width) [Fig. 4(c)]. Temperature dependence of the inelastic scattering at  $E = 1.4$  meV shows no anomaly at  $T_C$ , again suggesting no critical magnetic scattering.

While these results suggest that the FM phase transition in  $\text{CrI}_3$  may be weakly first order instead of second order<sup>14</sup>, a more stringent test is to measure the instantaneous spin correlations in  $\text{CrI}_3$  across  $T_C$ <sup>47</sup>. In these two-axis neutron scattering measurements, the final neutron wave vector is aligned along the  $c$ -axis direction throughout the scan and all final neutron energies are integrated [Fig. 4(e)]. For a classical second order phase transition, we expect to observe critical spin fluctuations as a peak in the instantaneous spin correlations at the  $(1, 1, 0)$  position, and the peak intensity should diverge on approaching  $T_C$  from high temperature. However, the temperature dependence of the scattering at the  $(1, 1, 0)$  position reveals no anomaly across  $T_C$  [Fig. 4(f)]. The wave vector dependence of the scattering at various temperature across  $T_C$  also shows no obvious peak at the  $(1, 1, 0)$  position. If we assume that the FM phase transition in  $\text{CrI}_3$  is indeed weakly first order instead of second order, we can understand the  $c$ -axis lattice distortion associated the FM phase transition<sup>14</sup> and the peak in FM transition induced heat capacity anomaly<sup>48</sup>. The first order nature of the FM transition in  $\text{CrI}_3$  provides a natural understanding for nonvanishing values of  $D(T)$  at  $T_C$ , suggesting that FM order is not controlled by the magnetic exchange interaction in contrast to a Heisenberg Hamiltonian<sup>4</sup>.

Another possible mechanism that can provide spin anisotropy gap in honeycomb ferromagnets is the symmetric off-diagonal  $\Gamma$  term in the  $J$ - $K$ - $\Gamma$  Hamiltonian<sup>18,22,23</sup>. Whereas it also originates from the

SOC, it is unlikely to be strong unless the diagonal  $K$  term is predominant. Figure 5(a) shows powder-averaged spin waves of  $\text{CrI}_3$  at  $T = 5$  K. To simulate the powder-averaged spin waves, we use linear spin wave theory with the SpinW software as discussed in<sup>49</sup>. For the calculated powder spectra shown in Figs. 5(b-d), the code chooses random orientation 1000 times to get an averaged intensity distribution.

The Heisenberg model Hamiltonian with DM interaction is

$$H = \sum_{i < j} [J_{ij} \mathbf{S}_i \cdot \mathbf{S}_j + \mathbf{A}_{ij} \cdot \mathbf{S}_i \times \mathbf{S}_j] + \sum_j D_z (S_j^z)^2 \quad (1)$$

as in ref.<sup>31</sup>, where  $J_{ij}$  is magnetic exchange coupling of the spin  $\mathbf{S}_i$  and  $\mathbf{S}_j$ ,  $\mathbf{A}_{ij}$  is the DM interaction between sites  $i$  and  $j$ , and  $D_z$  is the easy-axis anisotropy along the  $z$  ( $c$ ) axis. Figure 5(b) shows our simulated spin waves with the intralayer term  $J_1 = -2.13$  meV,  $J_2 = -0.09$  meV,  $J_3 = 0.10$  meV, interlayer term  $J_c = -0.59$  meV and anisotropy term  $D_z = -0.20$  meV. For the choice of the DM term  $A_{ij}$ , we used 0.194 meV in the calculation in Fig. 5(b). The DM term in ref.<sup>31</sup> ( $D_z = -0.31$  meV) is overestimated due to the poor sample mosaic.

The Heisenberg-Kitaev ( $J$ - $K$ - $\Gamma$ ) model Hamiltonian is

$$H = \sum_{\langle ij \rangle \in \lambda \mu (\nu)} [J_{ij} \mathbf{S}_i \cdot \mathbf{S}_j + K S_i^\nu S_j^\nu + \Gamma (S_i^\lambda S_j^\mu + S_i^\nu S_j^\lambda)], \quad (2)$$

where  $(\lambda, \mu, \nu) = \text{any permutation of } (x, y, z)$ . For the simulation reproducing that of<sup>18</sup>, we choose  $J_1 = -0.212$  meV for the Heisenberg term,  $K = -5.19$  meV for the Kitaev term, and  $\Gamma = -0.0675$  meV for the symmetric off-diagonal anisotropy. We keep the interlayer exchange term  $J_c$  the same as in the Heisenberg-DM model in Figs. 5(c,d,e).

As shown in Figs. 5(c,e), the model reproducing ref.<sup>18</sup> is clearly not consistent with the powder neutron scattering data because the model parameters give incorrect energy of the gap. The simplest way to solve the problem is to introduce next neighbor magnetic exchange  $J_2$  into the  $J$ - $K$ - $\Gamma$  Hamiltonian. To make optimal simulation using the  $J$ - $K$ - $\Gamma$  model, we fit the INS data in<sup>31</sup> with the  $J$ - $K$ - $\Gamma$  model, and the fitting result gives  $J_1 = -0.17$  meV,  $J_2 = -0.21$  meV,  $K = -5.6$  meV, and  $\Gamma = -0.075$  meV. Using these parameters, we get the simulation results in Fig. 5(d). These results suggest that the  $J$ - $K$ - $\Gamma$  model can have parameters regimes, similar to the Heisenberg-DM model in ref.<sup>31</sup>, that can describe the observed spin-wave spectra in  $\text{CrI}_3$ . The parameters in the new fit are similar to that in ref.<sup>18</sup>, except we must now introduce  $J_2$  in order to shift the Dirac gap from 5-8 meV to 10-13 meV. Figure 5(e) compares experimental data with Heisenberg-DM,  $J$ - $K$ - $\Gamma$  Hamiltonian with different fitting parameters along the boxed directions in 5(a-d), confirming that spin waves in  $\text{CrI}_3$  can be described by the  $J$ - $K$ - $\Gamma$  Hamiltonian but with parameters different from those in<sup>18</sup>.

### III. DISCUSSION

The direct relation between the magnetic anisotropy and FM phase transition is revealed in the similar temperature dependence of the spin gap  $\Delta(T)$  in Fig. 2(f) and magnetic order parameter in Fig. 1(e). The  $c$ -axis component of the ordered moment,  $S^z$ , is included in the anisotropic interaction term of the nearly-isotropic Heisenberg Hamiltonian  $H = -\sum_{i > j} J_{ij} \mathbf{S}_i \cdot \mathbf{S}_j - \sum_{\langle ik \rangle} A_{ik} S_i^z S_k^z$ , where  $\mathbf{S}_i$  is the spin on site  $i$ . The  $A_{ik}$  in the second term accounts for the single-ion anisotropy or anisotropic exchange constant, with  $c$  being the easy axis, when the summation is over  $i = k$  or  $i > k$ , respectively. If the anisotropic exchanges are limited to the nearest-neighbor bonds, the linear spin-wave energies calculated using  $A_{i > k} (\equiv A)$  are equal to those using the single-ion anisotropy  $A_{i=k} (= 3A)$ . Therefore, the resulting spin-wave spectra exhibiting anisotropy gap will also be indistinguishable. Regardless whether the spin gap is induced by single-ion or magnetic exchange anisotropy, the microscopic origin is the strong SOC induced by Cr-I interaction in  $\text{CrI}_3$ . Since the  $\text{CrI}_6$  octahedra has little structural distortions below  $T_C$ <sup>14</sup>, anisotropic Heisenberg exchange due to the SOC via Cr  $3d$ -I  $p$ -Cr  $3d$  superexchange path interaction is likely responsible for the FM order in  $\text{CrI}_3$ <sup>12,13</sup>.

Another possible mechanism that can provide spin anisotropy gap in honeycomb ferromagnets is the symmetric off-diagonal  $\Gamma$  term in the  $J$ - $K$ - $\Gamma$  Hamiltonian<sup>18,22,23</sup>. Whereas it also originates from the SOC, it is unlikely to be strong unless the diagonal  $K$  term is predominant. Although the  $J$ - $K$ - $\Gamma$  Hamiltonian with dominant Kitaev exchanges ( $K/J = 25$ )<sup>18</sup> fails to describe the spin-wave spectra, a reasonable fit to the full spectrum may be obtained when the next neighbor magnetic exchange  $J_2$  is allowed to be similar to  $J_1$ <sup>23</sup>.

### IV. CONCLUSIONS

In conclusion, we used INS to show that the stiffness of the intraplanar and interplanar spin waves of  $\text{CrI}_3$  has a finite value at  $T_C$ . While these results are contrary to the expectation of a 3D Heisenberg Hamiltonian with second order FM phase transition, they are consistent with our careful critical magnetic scattering measurements suggesting that the FM phase transition in  $\text{CrI}_3$  is a weakly first order transition. Since the anisotropy gap is fully closed at  $T_C$  following similar temperature dependence as the order parameter, we conclude that the anisotropic SOC plays a decisive role in the FM phase transition in 3D  $\text{CrI}_3$ , and is responsible for stabilizing the FM order in monolayer  $\text{CrI}_3$ . We are not aware a ferromagnet where the Curie temperature is controlled by SOC instead of the magnetic exchange coupling. Since spin waves in a ferromagnet are Goldstone modes, they are more unstable than spin waves in an antiferromagnet if there is no magnetic anisotropy. For example, it is well-known that

spin-wave-like excitations can appear above  $T_N$  in anti-ferromagnets, and temperature dependence of anisotropy gap follows the magnetic ordering parameter<sup>50,51</sup>. By judiciously adjusting the strength of SOC in 2D materials, one can control  $T_C$  of the system<sup>32-36</sup>. While monolayer  $\text{CrI}_3$  orders ferromagnetically at  $T_C \approx 45 \text{ K}$ <sup>8</sup>, monolayer  $\text{CrBr}_3$  can only order  $T_C \approx 34 \text{ K}$  due to the reduced SOC<sup>52</sup>, and long-range FM order will probably not survive in monolayer  $\text{CrCl}_3$ .

## V. ACKNOWLEDGMENTS

We are grateful to R. J. Birgeneau and Andriy Nev-  
idomskyy for helpful discussions. The INS and single  
crystal synthesis work at Rice was supported by the U.S.  
NSF Grant No. DMR-1700081 and the Robert A. Welch  
Foundation Grant No. C-1839 (P.D.), respectively. The  
work of J.-H.C. was supported by the National Research  
Foundation of Korea (No. NRF-2016R1D1A1B03934157;  
No. NRF2017K1A3A7A09016303). A portion of this re-  
search used resources at the Spallation Neutron Source, a  
DOE Office of Science User Facility operated by ORNL.  
Experiments at the ISIS Neutron and Muon Source were  
supported by a beam time allocation RB1820251 from  
the Science and Technology Facilities Council.

- 
- \* jaehc@korea.ac.kr  
† pdai@rice.edu
- <sup>1</sup> M. Gibertini, M. Koperski, A. F. Morpurgo, and K. S. Novoselov, *Nat. Nano.* **14**, 408 (2019).
  - <sup>2</sup> S. Lovesey in *Theory of Thermal Neutron Scattering from Condensed Matter*. (Clarendon, Oxford, 1984), Vol. 2.
  - <sup>3</sup> Jiandi Zhang, F. Ye, Hao Sha, Pengcheng Dai, J. A. Fernandez-Baca, and E. W. Plummer, *J. Phys.: Condens. Matter* **19**, 315204 (2007).
  - <sup>4</sup> M. Collins in *Magnetic Critical Scattering (Clarendon, Oxford)*, (1989).
  - <sup>5</sup> N. D. Mermin and H. Wagner, *Phys. Rev. Lett.* **17**, 1133 (1966).
  - <sup>6</sup> M. T. Hutchings, J. Als-Nielsen, P. A. Lindgard, and P. J. Walker, *J. Phys. C: Solid State Phys.* **14**, 5327 (1981).
  - <sup>7</sup> H. E. Stanley and T. A. Kaplan, *Phys. Rev. Lett.* **17**, 913 (1966).
  - <sup>8</sup> B. Huang, G. Clark, E. Navarro-Moratalla, D. R. Klein, R. Cheng, K. L. Seyler, D. Zhong, E. Schmidgall, M. A. McGuire, D. H. Cobden, W. Yao, D. Xiao, P. Jarillo-Herrero, and X. Xu, *Nature* **546**, 270 (2017).
  - <sup>9</sup> C. Gong, L. Li, Z. Li, H. Ji, A. Stern, Y. Xia, T. Cao, W. Bao, C. Wang, Y. Wang, Z. Q. Qiu, R. J. Cava, S. G. Louie, J. Xia, and X. Zhang, *Nature* **546**, 265 (2017).
  - <sup>10</sup> C. M. Wynn, M. A. Girtu, W. B. Brinckerhoff, K.-I. Sugiura, J. S. Miller, and A. J. Epstein, *Chem. Mater.* **9**, 2156 (1997).
  - <sup>11</sup> B. D. Cullity and C. D. Graham, *Introduction to Magnetic Materials*. (John Wiley & Sons, 2005).
  - <sup>12</sup> J. L. Lado and J. Fernández-Rossier, *2D Materials* **4**, 035002 (2017).
  - <sup>13</sup> Dong-Hwan Kim, Kyoo Kim, Kyung-Tae Ko, JunHo Seo, Jun Sung Kim, Tae-Hwan Jang, Younghak Kim, Jae-Young Kim, Sang-Wook Cheong, and Jae-Hoon Park, *Phys. Rev. Lett.* **122**, 207201 (2019).
  - <sup>14</sup> M. A. McGuire, H. Dixit, V. R. Cooper, and B. C. Sales, *Chem. Mater.* **27**, 612 (2015).
  - <sup>15</sup> Jeffrey G. Rau, Eric Kin-Ho Lee, and Hae-Young Kee, *Phys. Rev. Lett.* **112**, 077204 (2014).
  - <sup>16</sup> Heung-Sik Kim, Vijay Shankar V., Andrei Catuneanu, and Hae-Young Kee, *Phys. Rev. B* **91**, 241110(R) (2015).
  - <sup>17</sup> P. Peter Stavropoulos, D. Pereira, and Hae-Young Kee, *Phys. Rev. Lett.* **123**, 037203 (2019).
  - <sup>18</sup> I. Lee, F. G. Utermohlen, K. Hwang, D. Weber, C. Zhang, J. V. Tol, J. E. Goldberger, N. Trivedi, and P. C. Hammel, *Phys. Rev. Lett.* **124**, 017201 (2020).
  - <sup>19</sup> Changsong Xu, Junsheng Feng, Hongjun Xiang, and Laurent Bellaiche, *npj Comp. Mater.* **4**, 57 (2018).
  - <sup>20</sup> Moumita Deb and Asim Kumar Ghosh, *J. Phys.: Condens. Matter* **31**, 345601 (2019).
  - <sup>21</sup> Darshan G. Joshi, *Phys. Rev. B* **98**, 060405(R) (2018).
  - <sup>22</sup> P. Lampen-Kelley, S. Rachel, J. Reuther, J.-Q. Yan, A. Banerjee, C. A. Bridges, H. B. Cao, S. E. Nagler, and D. Mandrus, *Phys. Rev. B* **98**, 100403(R) (2018).
  - <sup>23</sup> See supplementary information for additional data and analysis.
  - <sup>24</sup> N. Richter, D. Weber, F. Martin, N. Singh, U. Schwingenschlögl, B. V. Lotsch, and M. Kläui, *Phys. Rev. Mater.* **2**, 024004 (2018).
  - <sup>25</sup> J. W. Lynn, R. W. Erwin, J. A. Borchers, Q. Huang, A. Santoro, J.-L. Peng, and Z. Y. Li, *Phys. Rev. Lett.* **76**, 4046 (1996).
  - <sup>26</sup> J. A. Fernandez-Baca, P. Dai, H. Y. Hwang, C. Kloc, and S.-W. Cheong, *Phys. Rev. Lett.* **80**, 4012 (1998).
  - <sup>27</sup> J. H. E. Griffiths, *Nature (London)* **158**, 670 (1946).
  - <sup>28</sup> A. T. Abdalian, B. Briat, C. Dugautier, and P. Moch, *J. Phys. C: Solid State Phys.* **20**, 2465 (1987).
  - <sup>29</sup> J. F. Dillon and C. E. Olson, *J. Appl. Phys.* **36**, 1259 (1965).
  - <sup>30</sup> Wencan Jin, Hyun Ho Kim, Zhipeng Ye, Siwen Li, Pouyan Rezaie, Fabian Diaz, Saad Siddiq, Eric Wauer, Bowen Yang, Chenghe Li, Shangjie Tian, Kai Sun, Hechang Lei, Adam W. Tsen, Liuyan Zhao, and Rui He, *Nat. Comm.* **9**, 5122 (2018).
  - <sup>31</sup> Lebing Chen, Jae-Ho Chung, Bin Gao, Tong Chen, Matthew B. Stone, Alexander I. Kolesnikov, Qingzhen Huang, and Pengcheng Dai, *Phys. Rev. X* **8**, 041028 (2018).
  - <sup>32</sup> Yujun Deng, Yijun Yu, Yichen Song, Jingzhao Zhang, Nai Zhou Wang, Zeyuan Sun, Yangfan Yi, Yi Zheng Wu, Shiwei Wu, Junyi Zhu, Jing Wang, Xian Hui Chen, and Yuanbo Zhang, *Nature* **563**, 94 (2018).
  - <sup>33</sup> Zaiyao Fei, Bevin Huang, Paul Malinowski, Wenbo Wang, Tiancheng Song, Joshua Sanchez, Wang Yao, Di Xiao, Xi-aoyang Zhu, Andrew F. May, Weida Wu, David H. Cobden, Jiun-Haw Chu, Xiaodong Xu, *Nature Materials* **17**, 778 (2018).



- <sup>34</sup> Manuel Bonilla, Sadhu Kolekar, Yujing Ma, Horacio Coy Diaz, Vijaysankar Kalappattil, Raja Das, Tatiana Eggers, Humberto R. Gutierrez, Manh-Huong Phan, Matthias Batzill, *Nature Nanotechnology* **13**, 289 (2018).
- <sup>35</sup> D. J. OHara, T. Zhu, A. H. Trout, A. S. Ahmed, Y. K. Luo, C. H. Lee, M. R. Brenner, S. Rajan, J. A. Gupta, D. W. McComb, and R. K. Kawakami, *Nano Letters* **18**, 3125 (2018).
- <sup>36</sup> M. Gibertini, M. Koperski, A. F. Morpurgo, and K. S. Novoselov, *Nat. Nanotechnology* **14**, 408 (2019).
- <sup>37</sup> R. I. Bewley, J. W. Taylor, S. M. Bennington, *Nuclear Instruments and Methods in Physics* **637**, 128 (2011).
- <sup>38</sup> R. A. Ewings, A. Buts, M. D. Le, J. van Duijn, I. Bustinduy, T. G. Perring, *Nuclear Instruments and Methods in Physics Research A* **834**, 132 (2016).
- <sup>39</sup> M. A. McGurie, *Crystal* **7**, 121 (2017).
- <sup>40</sup> Heinz Maier-Leibnitz Zentrum, *Journal of Large-Scale Research Facilities*, **1**, A12 (2015).
- <sup>41</sup> D. H. Yu, R. Mole, T. Noakes, S. Kennedy, and R. Robinson, *J. Phys. Soc. Jpn.* **82**, SA027 (2013).
- <sup>42</sup> G. E. Granroth, A. I. Kolesnikov, T. E. Sherline, J. P. Clancy, K. A. Ross, J. P. C. Ruff, B. D. Gaulin, S. E. Nagler, *Journal of Physics: Conference Series* **251**, 12058 (2010).
- <sup>43</sup> Barry Winn, Uwe Filges, V. Ovidiu Garlea, Melissa Graves-Brook, Mark Hagen, Chenyang Jiang, Michel Kennemann, Larry Passell, Stephen M. Shapiro, Xin Tong, and Igor Zaliznyak, *EPJ Web of Conferences* **83**, 03017 (2015).
- <sup>44</sup> A. R. Wildes, H. M. Rønnow, B. Roessli, M. J. Harris, and K. W. Godfrey, *Phys. Rev. B* **74**, 094422 (2006).
- <sup>45</sup> E. J. Samuelsen, R. Silbergliitt, G. Shirane, and J. P. Remika, *Phys. Rev. B* **3**, 157 (1971).
- <sup>46</sup> T. J. Williams, A. A. Aczel, M. D. Lumsden, S. E. Nagler, M. B. Stone, J.-Q. Yan, and D. Mandrus, *Phys. Rev. B* **92**, 144404 (2015).
- <sup>47</sup> R. J. Birgeneau, M. Greven, M. A. Kastner, Y. S. Lee, B. O. Wells, Y. Endoh, K. Yamada, and G. Shirane, *Phys. Rev. B* **59**, 13788 (1999).
- <sup>48</sup> G. T. Lin, X. Luo, F. C. Chen, J. Yan, J. J. Gao, Y. Sun, W. Tong, P. Tong, W. J. Lu, Z. G. Sheng, W. H. Song, X. B. Zhu and Y. P. Sun, *Appl. Phys. Lett.* **112**, 072405 (2018).
- <sup>49</sup> S. Toth and B. Lake, *Journal of Physics: Condensed Matter* **27**, 16 (2015).
- <sup>50</sup> H. W. de Wijn, L. R. Walker, S. Geschwind, and H. J. Guggenheim, *Phys. Rev. B* **8**, 299 (1973).
- <sup>51</sup> Franz Demmel and Tapan Chatterji, *Phys. Rev. B* **76**, 212402 (2007).
- <sup>52</sup> Zhaowei Zhang, Jiangzhi Shang, Chongyun Jiang, Abdullah Rasmita, Weibo Gao, and Ting Yu, *Nano Lett.* **19**, 3138 (2019).